Atomic-layer-deposited ultrafine MoS_2 nanocrystals on cobalt foam for efficient and stable electrochemical oxygen evolution

Dehua Xiong,[a,b] Qingqing Zhang,[b] Wei Li,[a] Junjie Li,[a] Xiuli Fu,[c] M. F. Cerqueira,[d] Pedro Alpuim[a,d] and Lifeng Liu[*a]

[a]International Iberian Nanotechnology Laboratory (INL), Av. Mestre Jose Veiga, 4715-330 Braga, Portugal. E-mail: lifeng.liu@inl.int
[b]State Key Laboratory of Silicate Materials for Architectures, Wuhan University of Technology, Wuhan 430070, P. R. China
[c]State Key Laboratory for Information Photonics & Optical Communications and School of Science, Beijing University of Posts & Telecommunications, Beijing 100876, P. R. China
[d]Center of Physics, University of Minho, 4710-057 Braga, Portugal

Abstract

Ultrafine molybdenum sulfide (MoS_2) nanocrystals are grown on a porous cobalt (Co) foam current collector by atomic layer deposition (ALD) using molybdenum hexacarbonyl and hydrogen sulfide as precursors. When used to catalyze the oxygen evolution reaction (OER), the optimal Co@MoS_2 electrode, even with a MoS_2 loading as small as 0.06 mg cm^{-2}, exhibits a large cathodic shift of ca. 200 mV in the onset potential (the potential at which the current density is 5 mA cm^{-2}), a low overpotential of only 270 mV to attain an anodic current density of 10 mA cm^{-2}, much smaller charge transfer resistance and substantially improved long-term stability at both low and high current densities, with respect to the bare Co foam electrode, showing substantial promise for use as an efficient, low-cost and durable anode in water electrolyzers.

The ever-growing energy demand and the increasing concern about environmental pollution impel researchers to explore highly efficient and affordable catalysts for clean and sustainable energy generation, especially for electrocatalytic water splitting into hydrogen (H_2) and oxygen (O_2), which represents a promising solution to providing renewable H_2 fuels.[1] Compared to the H2 evolution reaction (HER), the O_2 evolution reaction (OER) is more thermodynamically and kinetically demanding and has been regarded as the bottleneck of electrochemical water splitting. Without a catalyst, OER will occur at a high overpotential leading to significant losses in the energy efficiency of electrolysis. Noble metal oxides such as iridium and ruthenium oxides (IrO_2 and RuO_2) have been demonstrated to be the state-of-the-art electrocatalysts for OER.[2,3] However, the scarcity and high cost of noble metals limit their large-scale employment in practical water splitting devices. Therefore, considerable effort has recently been made in the search for highly active, durable, non-precious OER catalysts comprising earth-abundant elements,[4,5] including transition metal oxides,[6,7] hydroxides,[8] sulfides,[6,9–11] selenides[12,13] and recently developed phosphides.[14–20]

Molybdenum sulfides with different stoichiometries and polymorphs have been intensively investigated in the past decade as alternative catalysts to noble metals.[21–26] However, virtually all these studies were focused on the catalysis for HER, and the possibility of utilizing molybdenum sulfides as OER catalysts has not been explored until very recently.[27–30.] In early 2016, Wu et al. reported that chemically exfoliated 1T-MoS_2 shows excellent electrocatalytic performance for OER an acidic medium, with a relatively small overpotential (η) to attain an anodic current density of 10 mA cm^{-2}.[27] Zhu and coworkers also demonstrated that MoS_2 nanoplates perpendicularly grown on carbon nanofibers (CNFs) are active towards the OER, but their activity is markedly lower than that of the Co_9S_8@MoS_2 core–shell nanostructures they synthesized.[28] Lately, Zhang et al. also observed significantly enhanced catalytic activity for OER delivered by MoS_2/Ni_3S_2 heterostructures with abundant interfaces. According to their density functional theory (DFT) calculations, they concluded that the MoS_2/Ni_3S_2 interfaces

synergistically favor the chemisorption of oxygen-containing intermediates, thus promoting the OER.[29] Although in these previous studies researchers have demonstrated that hybrid structures consisting of MoS2 interfaced with Co or Ni sulfide have excellent activity towards the OER, they also pointed out that pure MoS_2 is an inefficient OER catalyst.[28,29]

Herein, we report the atomic layer deposition (ALD) of ultrafine MoS_2 nanocrystals (NCs) over a porous cobalt (Co) foam current collector and their outstanding electrocatalytic performance towards the OER. ALD is a very powerful technique enabling conformal deposition of thin films/NPs on nonplanar high aspect ratio substrates.[31] Unlike transition metal oxides, reports on the ALD of molybdenum sulfides are very limited because of the lack of suitable chemistry for ALD.[32–35]

Previously, molybdenum chloride ($MoCl_5$) and hydrogen sulfide (H_2S)[32] as well as molybdenum hexacarbonyl ($Mo(CO)_6$) and dimethyl disulfide (DMDS)[33–35] have been employed as Mo and S precursors, respectively. In this work, we use $Mo(CO)_6$ and H2S as precursors to directly deposit ultrafine MoS_2 NCs on Co foam ($Co@MoS_2$), and for the first time investigate the OER performance of ALD-derived MoS_2. The $Co@MoS_2$ subjected to 500 ALD cycles (with a MoS_2 loading mass of 0.06 mg cm^{-2}) exhibits outstanding OER activity requiring an overpotential of only 270 mV to deliver a current density of 10 mA cm^{-2}, being one of the best-performing sulfide-based OER electrocatalysts and favorably comparable to the state-of-the-art noble metal electrocatalysts reported in the literature. Furthermore, the $Co@MoS_2$ electrode can operate at 20 mA cm^{-2} for 50 hours and at 100 mA cm^{-2} for an additional 50 hours without noticeable degradation, showing excellent long-term stability.

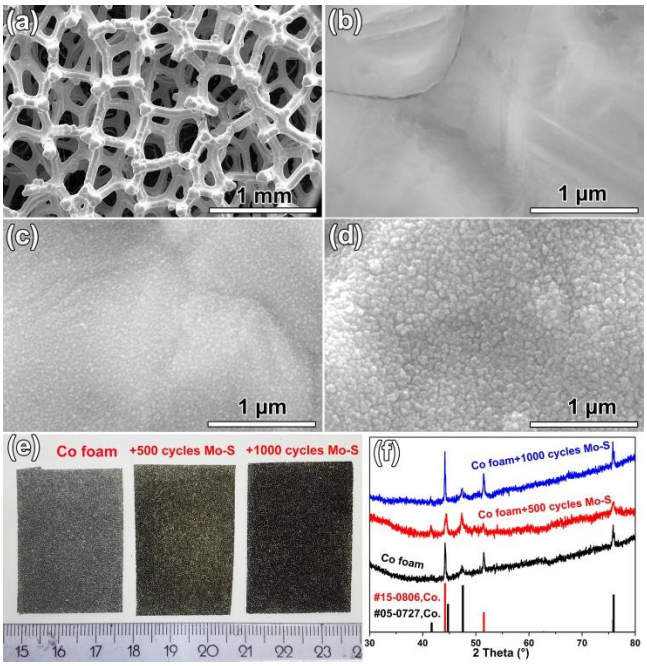

Fig. 1 SEM images of (a, b) a bare Co foam, (c) $Co@MoS_2$-500, and (d) $Co@MoS_2$-1000. (e) Digital photographs and (f) XRD patterns of the bare Co foam, $Co@MoS_2$-500 and $Co@MoS_2$-1000 electrodes.

Fig. 1a shows a scanning electron microscopy (SEM) image of a bare Co foam, where the macroporous feature can be clearly seen. A close inspection reveals that the Co ligaments have a relatively smooth surface (Fig. 1b). X-ray diffraction (XRD) examination confirms that the Co foam consists of two crystalline phases, namely, face-centered-cubic Co (fcc Co, JCPDS no. 15-0806) and hexagonal-close-packed Co (hcp Co, JCPDS no. 05-0727), as evidenced by the characteristic diffraction peaks located at 44.2°, 47.3°, 51.5°, and 75.8°, respectively (Fig. 1f). After the ALD of MoS_2, the surface of the Co foam was found to be uniformly covered with many small nanoparticles (NPs) (Fig. 1c, d, S1 and S2, ESI†), and energy-dispersive X-ray spectroscopy (EDX) measurements confirmed the existence of Mo and S elements on the Co foam surface (Fig. S3 and S4, ESI†). The NP size increases with the increasing ALD cycle number. Typically, the NPs are 10–20 nm in size when 500 cycles of ALD are performed (denoted as $Co@MoS_2$-500, Fig. 1c); while when the ALD cycle number is increased to 1000 (denoted as $Co@MoS_2$-1000), the NP size markedly goes up to 30–40 nm (Fig. 1d). In terms of appearance, the

original light grey Co foam becomes dark after the ALD of MoS_2 (Fig. 1e). A similar change was also observed on the glass slide that was placed together with the Co foam substrate in the ALD reactor (Fig. S5, ESI†), indicating the successful deposition of MoS_2. However, the XRD examination of Co@MoS_2 electrodes doesn't show any visible diffraction peaks other than those arising from metallic Co (Fig. 1f), suggesting that either the crystallite size of ALD-derived MoS_2 is too small or the amount of the deposited MoS_2 is too low to be detected by XRD.

To gain further insight into the microstructure and composition of MoS_2 NCs, a transmission electron microscopy (TEM) examination was carried out. Fig. 2a shows a representative TEM image, where lots of ultrafine NPs with a diameter of ca. 5 nm can be unambiguously resolved. It is worth noting that the dimension of these NPs is smaller than the apparent size of NPs that we observed using SEM (Fig. 1c and S1, ESI†), implying that MoS_2 was grown on the Co foam surface in the form of aggregates of nanocrystallites, which then split into ultrafine NCs upon ultrasonication treatment prior to the TEM examination. High-resolution TEM (HRTEM) analysis clearly illustrates the lattice structure of $MoS_2$2 NCs (Fig. 2b), and the measured interplanar spacing is about 0.269 nm, corresponding to the distance of (100) crystal planes of hexagonal MoS_2 (2H- MoS_2). Fast Fourier-transformation electron diffraction (FFT-ED) analysis (Fig. 2b, inset) over a big NC reveals a well-defined spotted pattern that can be assigned to the diffractions along the [001] zone axis of hexagonal MoS2 (JCPDS no.37-1492), indicating that this NC is single-crystalline. Extensive EDX analyses over either a single NC or NC agglomerates show that the NCs consist primarily of Mo and S (Fig. 2c). The Cu and C peaks originate from the TEM grid used, and the O signal may arise from the absorbed oxygen or the remnant of the $Mo(CO)_6$ precursor. Furthermore, elemental mapping was performed in the high-angle annular dark-field scanning transmission electron microscopy (HAADF-STEM) mode. The ultrafine NCs and their aggregates can be seen more clearly in the HAADF-STEM image (Fig. 2d), and Mo and S elements are found to be distributed over the NCs evenly (Fig. 2d–f).

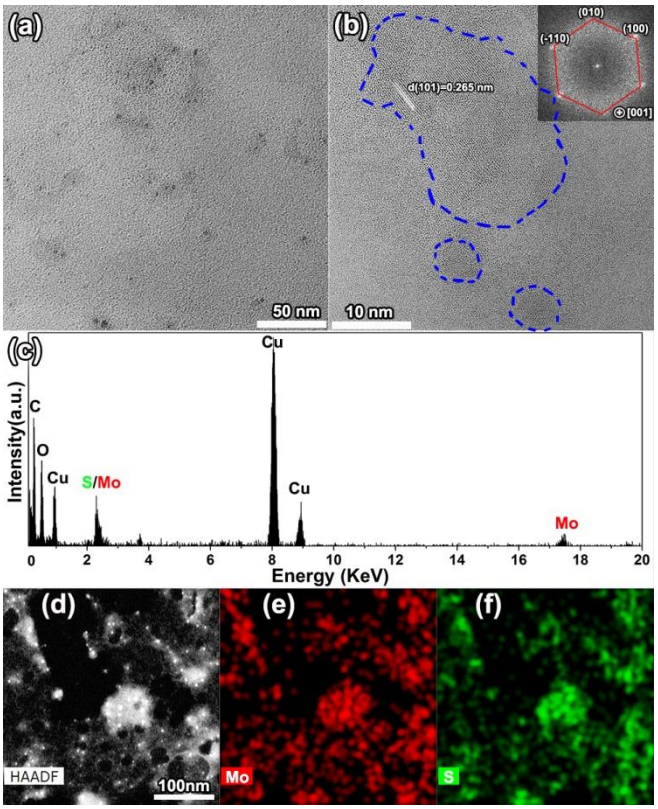

Fig. 2 TEM characterization of ALD-derived MoS_2 NCs. (a) Lowmagnification and (b) high-resolution TEM (HRTEM) images. MoS_2 NCs are indicated by the blue dotted lines. The inset of (b) is the Fouriertransformation ED pattern over the large blue dotted line enclosed area. (c) EDX spectrum. (d–f) HAADF-STEM and elemental maps of Mo (K_α:17.44 keV) and S (K_α:2.31 keV). Scale bars: 100 nm.

The surface chemical state of Co@ MoS_2-500 was further investigated by X-ray photoelectron spectroscopy (XPS). Fig. 3 shows the high-resolution XPS spectra of Mo 3d and S 2p. In the Mo 3d spectrum, two peaks located at the binding energy (BE) values of 229.7 and 232.3 eV can be assigned to

the Mo $3d_{5/2}$ and Mo $3d_{3/2}$ core levels, respectively; while the peak at 226.5 eV is associated with the S 2s core level (Fig. 3a), which agrees with previous reports on MoS_2 and confirms the Mo^{4+} and S^{2-} charge states occur due to Mo–S charge transfer.[36] Another peak located at 235.4 eV is also ascribed to Mo $3d_{3/2}$, indicative of an oxidation state of +6. This is likely caused by the oxidation of MoS_2 upon exposure to the air. Fig. 3b presents the core-level spectrum of the S 2p region with two main peaks and one shake-up satellite, in which the peaks at BE values of 161.9 and 163.1 eV correspond to S $2p_{3/2}$ and S $2p_{1/2}$, respectively. The single doublet with the $2p_{3/2}$ peak located at 161.9 eV indicates an oxidation state of -2 for sulfur. Furthermore, Raman spectroscopy measurement was also carried out on Co@ MoS_2-1000, and two distinct peaks at 380 cm^{-1} and 407 cm^{-1} were observed, which can be assigned to the E_{12g} and A_{1g} vibrational modes of MoS_2,[37] respectively (Fig. S6, ESI†). The Raman result in combination with the XPS and TEM characterization unambiguously illustrates that the ALD-derived NCs are hexagonal MoS_2.

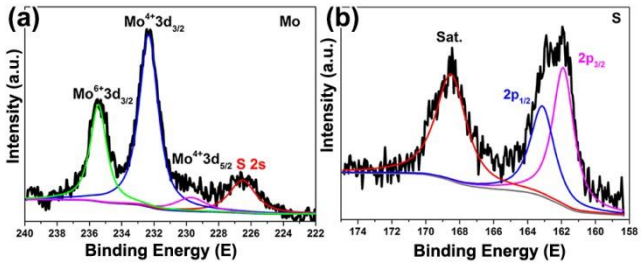

Fig. 3 Mo 3d (a) and S 2p (b) XPS spectra of the Co@MoS_2-500.

The electrocatalytic performance of Co@ MoS_2 electrodes towards the OER was evaluated in O_2-saturated 1.0 M KOH solution using linear scan voltammetry (LSV). Fig. 4a shows the LSV curves of Co@ MoS_2-500 and Co@ MoS_2-1000. For comparison, the OER activity of a bare Co foam was also measured. As shown in Fig. 3a, the bare Co foam only shows a very small anodic current up to 1.63 V *vs.* RHE. Upon loading with MoS_2 NPs, the OER onset potential (the potential at which the anodic current density is 5 mA cm^{-2}) is substantially shifted cathodically by *ca.* 200 mV and 120 mV for Co@ MoS_2-500 and Co@ MoS_2-1000, respectively. The Co@ MoS_2-500 electrode only needs overpotentials of 270 mV (η10) and 300 mV (η_{20}), respectively, to attain current densities of 10 and 20 mA cm-2, which are superior to those of many other sulfide-based OER electrocatalysts such as hollow Co_3S_4 nanosheets (ηonset = 363 mV),[38] ultrathin Co_3S_4 nanosheets (η_{onset} = 355 mV) and bulk Co_3S_4 (η_{onset} = 590 mV),[39] Co_9S_8/CNFs (η_{10} = 512 mV), Co_9S_8@ MoS_2/CNFs (η_{10} = 430 mV) and MoS_2/CNFs (η_{onset} = 432 mV),[28] Co_9S_8/N-doped carbon (η_{10} = 320 mV),[40] Ni_3S_2/N-doped carbon (η_{10} = 390 mV),[40] and Co_3O_4 nanosheet/ex-MoS_2(η_{10} =350 mV),[41] as well as the state-of-the-art RuO_2 (η_{10} = 380 ± 20 mV) and IrO2 (η_{10} = 380 ± 10 mV) nanoparticulate catalysts recently reported in the literature[42] (Table S1, ESI†). Similarly, Co@ MoS_2-1000 also exhibits remarkably enhanced OER activity with respect to the bare Co foam, though it is slightly inferior to Co@ MoS_2-500. To further confirm that the high OER activity indeed results from MoS_2, a control experiment was carried out where an ALD sequence, the same as that for Co@ MoS_2-500, was used but without the supply of the Mo sources (i.e., only H_2S was exposed to the Co foam for 500 half cycles). The thus-obtained electrode (denoted as Co@H_2S-500) showed OER activity even inferior to that of the bare Co foam (Fig. S7 and S8, ESI†). The control experiment explicitly shows that the ALD-derived MoS_2 NCs are the effective species responsible for enhanced electrocatalytic activity towards the OER. To gain an additional understanding of the OER kinetics, Tafel analysis was performed (Fig. 4b). The Tafel slopes of Co@ MoS_2-500 and Co@ MoS_2-1000 are 74 and 61 mV dec^{-1}, respectively, which favorably compare to those of other sulfide-based OER catalysts (Table S1, ESI†). However, the Tafel slope of the Co@ MoS_2 electrodes is found to be higher than that of the bare Co foam (41 mV dec^{-1}), which presumably results from the relatively poor electrical conductivity of the deposited MoS_2 NC films.

Electrochemical impedance spectroscopy (EIS) was further used to investigate the charge transfer kinetics at the catalyst/electrolyte interface during the OER. Fig. 4c displays the Nyquist plots of the bare Co foam, Co@ MoS_2-500 and Co@ MoS_2-1000 electrodes, which can be fitted using an equivalent circuit model consisting of an equivalent series resistance (Rs), and two parallel combinations of a resistance and a constant phase element in series (Fig. 4d), corresponding to the charge transport process occurring at the Co/ MoS_2 interface (R_{sc}-CPE1) and the charge transfer taking place at the MoS_2/electrolyte interface (R_{ct}-

CPE2), respectively. According to the fitting results (Table S2, ESI†), the charge transfer resistance (R_{ct}) of Co@ MoS_2-500 and Co@MoS_2-1000 is only 0.58 and 1.95 Ω cm^{-2}, respectively, significantly smaller than that of the bare Co foam (11.31 Ω cm^{-2}), suggesting that ultrafine MoS_2 NCs dramatically expedite the OER process.

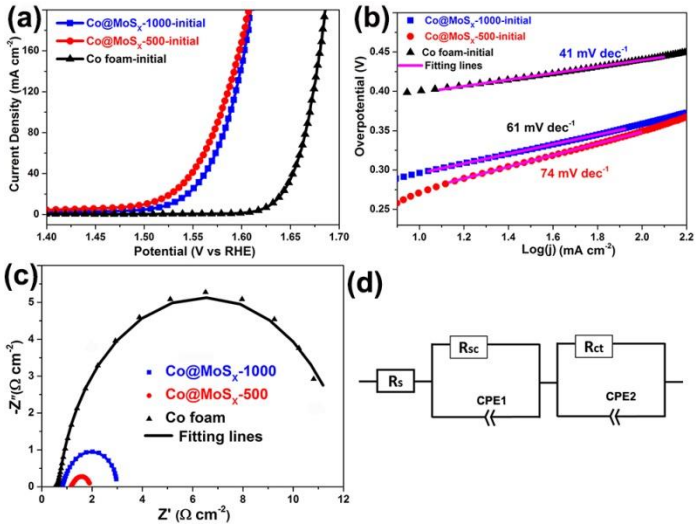

Fig. 4 (a) *iR*-Corrected polarization curves of the bare Co foam, Co@MoS_2-500 and Co@MoS_2-1000 electrodes recorded in 1 M KOH solution at a scan rate of 5 mV s^{-1}. (b) Tafel plots. (c) Nyquist plots (solid lines are fitting curves). (d) Equivalent circuit model used for fitting. All measurements were performed at room temperature (~25 °C).

It is now generally accepted that the edge planes of layered MoS_2 are responsible for its HER activity, where the free energy of H2 adsorption is theoretically close to that of Pt.[22] However, the catalytically active sites of MoS_2 for the OER remain elusive for the time being. Compared to HER, OER is a more complicated reaction and it involves four primary steps with three adsorbed intermediates, i.e., *OH, O*, and *OOH, interacting in a similar way at the catalyst surface. Recent density functional theory (DFT) calculations have proposed that the OER activity of MoS_2 may result from edge sites as well rather than basal plane sites.[27] The ultrafine features of ALD-MoS_2 NCs reported here would advantageously facilitate the exposure of edge sites, which could reasonably explain the outstanding catalytic activity observed for the OER.

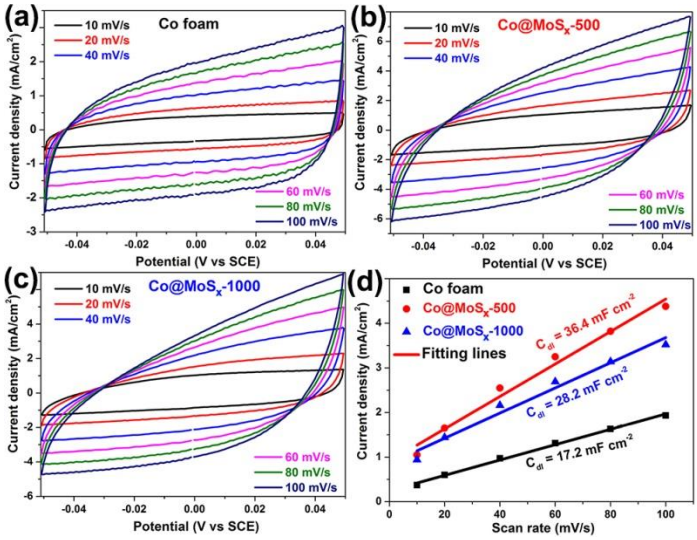

Fig. 5 (a–c) CV curves of the bare Co foam, Co@MoS_2-500 and Co@MoS_2-1000 electrodes measured in 1 M KOH in the non-Faradaic region with different scan rates from 10 to 100 mV s_{-1}. (d) Half of the difference between anodic and cathodic current densities ($\Delta J = (J_a - J_c)/2$) at 0 V vs. SCE plotted against the scan rate. The linear slope is equivalent to the double-layer capacitance C_{dl} that is proportional to the ECSA.

The high electrochemically active surface area (ECSA) of the Co@ MoS_2 electrodes was verified by measuring the electrochemical double-layer capacitance (C_{dl}), given the fact that C_{dl} is proportional to the ECSA. The C_{dl} was obtained through cyclic voltammetric scans in the non-faradaic potential window of -0.05 V–0.05 V *vs.* SCE at different rates ranging from 10 to 100 mV s-1 (Fig. 5a–c).[43] As is shown in Fig. 5d, the C_{dl} values calculated for the bare Co foam, Co@ MoS_2-500 and Co@ MoS_2-1000 are 17.2, 36.4 and 28.2 mF cm^{-2}, respectively. The C_{dl}, and thereby the ECSA, of Co@ MoS_2-500 is higher than that of Co@MoS2-1000, which likely arises from the smaller NP size of Co@ MoS_2-500 (Fig. 1) and can reasonably explain why Co@ MoS_2-500 has a higher OER activity than Co@ MoS_2-1000 (Fig. 4a) even if the MoS_2 loading on the former is smaller (Table S1, ESI†). It is also noted that the C_{dl} of Co@MoS2-500 is double that of the bare Co foam. However, the high ECSA alone cannot fully account for the significantly enhanced anodic current of Co@ MoS_2-500 relative to that of the bare Co foam at a given potential. For example, at η = 350 mV, Co@ MoS_2-500 delivers a current density of ca. 105.6 mA cm^{-2}, significantly higher than 0.7 mA cm^{-2} delivered by the bare Co foam at the same potential. This indicates that MoS_2 possesses much intrinsically higher electrocatalytic activity for the OER.

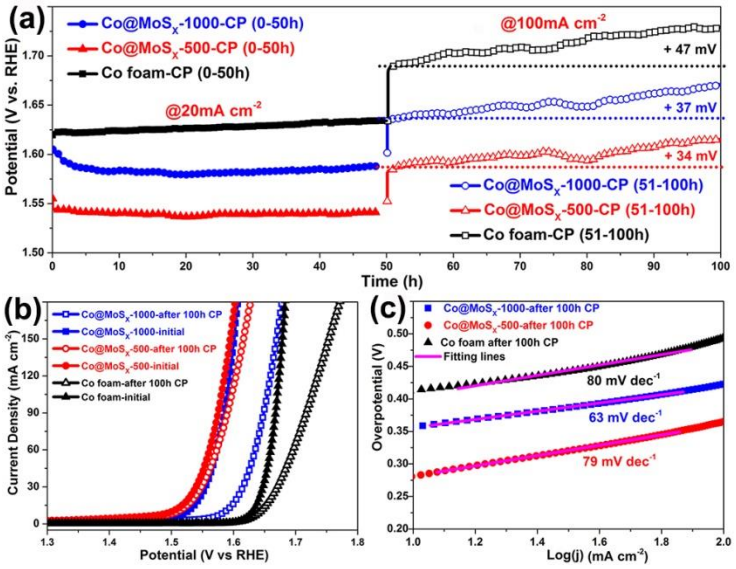

Fig. 6. (a) Chronopotentiometric curves of the bare Co foam, Co@MoS_2-500 and Co@MoS_2-1000 electrodes measured at 20 and 100 mA cm^{-2}. (b) Polarization curves of the electrodes recorded before and after the CP test. Scan rate: 5 mV s^{-1}. (c) Tafel plots of the electrodes after the 100 h CP test. Solid lines are fitting curves.

Long-term stability is an important criterion for OER catalysts in terms of their practical applications. The long-term stability of Co@ MoS_2 electrodes was examined by chronopotentiometry (CP) at a constant current density of 20 mA cm^{-2} for 50 hours, followed by a continued test at an industry relevant high current density of 100 mA cm^{-2} for another 50 hours. As shown in the CP curves in Fig. 6a, to maintain 20 mA cm^{-2}, the Co@ MoS_2-500 electrode only needs a potential of 1.54 V *vs.* RHE (i.e., η_{20} = 310 mV), consistent with that extracted from the LSV curve (Fig. 4a). Moreover, the potential remains constant during the 50 h galvanostatic electrolysis. The Co@ MoS_2-1000 electrode needs a slightly higher potential of 1.58 V to deliver 20 mA cm^{-2} (i.e., η_{20} = 350 mV), but the overpotential that is needed virtually doesn't increase upon continuous electrolysis, similarly to that of Co@ MoS_2-500. In contrast, a much higher η_{20} is demanded for the bare Co foam electrode, and η_{20} also increases, though slowly, over time, reaching 404 mV after 50 h. At the high current of 100 mA cm^{-2}, all electrodes show an overpotential increase after continuous electrolysis for 50 h, the amplitude of which follows the order: Co foam (47 mV) > Co@ MoS_2-1000 (37 mV) > Co@ MoS_2-500 (34 mV). Nevertheless, η_{100} of the Co@ MoS_2-500 (i.e., 380 mV) is still remarkably smaller than that of the Co foam, showing better OER activity. After an extended stability test for 100 h, both the bare Co foam and Co@ MoS_2 show a reduction in activity, to a certain extent. However, the LSV curve of Co@ MoS_2-500 only slightly drifts positively, whereas the LSV curves of Co@ MoS_2-1000 and the bare Co foam exhibit a large positive shift with respect to the initial polarization curves (Fig. 6b and S9, ESI†). Tafel analysis reveals that the Tafel slopes of Co@ MoS_2-500 and Co@ MoS_2-1000 only vary slightly, indicating a similar OER

kinetics even after the long-term stability test, while the Tafel slope of the bare Co foam substantially increases from 41 to 80 mV dec^{-1}, implying that the OER occurs more slowly on the Co foam after the long term CP test (Fig. 6c). This might arise from the generation of poorly conductive cobalt oxy-hydroxide over the entire surface of the Co foam, as is discussed below. The long-term stability of the Co@H_2S-500 electrode was also examined, and found to be even inferior to that of the bare Co foam (Fig. S8, ESI†). This again confirms that the outstanding catalytic performance of Co@ MoS_2 electrodes should be explained by the deposited ultrafine MoS_2 NCs.

The morphology, crystal structure and composition of the electrodes after the long-term stability test for 100 h (i.e., 50 h at 20 mA cm^{-2} followed by 50 h at 100 mA cm^{-2}) were examined using SEM, XRD and Raman spectroscopy. As shown in Fig. 7a and b, nanosheet-like structures appear on the entire surface of the bare Co foam after OER. These nanosheets are well-crystallized and can be assigned to CoOOH according to our TEM analyses (Fig. S10, ESI†). Extensive EDX analyses indeed verified that there was a strong peak from O in the post-OER Co foam (Fig. 7c). However, according to our XRD examination no crystal phases from CoOOH were observed (Fig. S11, ESI†), implying that the amount of CoOOH was probably too low to be resolved by XRD. Compared to the bare Co foam, the morphology of Co@ MoS_2 virtually did not change after the 100 h CP test (Fig. 7d, e, g and h), except that some cracks were observed on the surface of Co@ MoS_2. In particular, the cracks appearing on Co@ MoS_2-1000 are more abundant and larger than those on Co@ MoS_2-500. It is worth noting that no nanosheets were observed on Co@MoS2 electrodes. However, EDX analyses showed an O peak in both Co@ MoS_2-500 and Co@ MoS_2-1000 after the stability test (Fig. 7f and i), remarkably stronger than that of the as-prepared Co@ MoS_2 electrodes (Fig. S3 and S4, ESI†), indicating that the MoS_2 was oxidized. Nevertheless, signals from Mo and S are still visible though the peak intensity was substantially attenuated. XRD analyses show no diffraction peaks other than metallic Co (Fig. S11, ESI†). However, Raman spectroscopy measurements (Fig. S12, ESI†) demonstrate the presence of MoO_3, confirming the transformation of MoS_2 to molybdenum oxide under OER conditions in the alkaline solution. This transformation was also observed previously in MoS_2 microspheres after repetitive anodic CV scans[30] and it happens generally for all sulfide-based OER catalysts.[44,45]

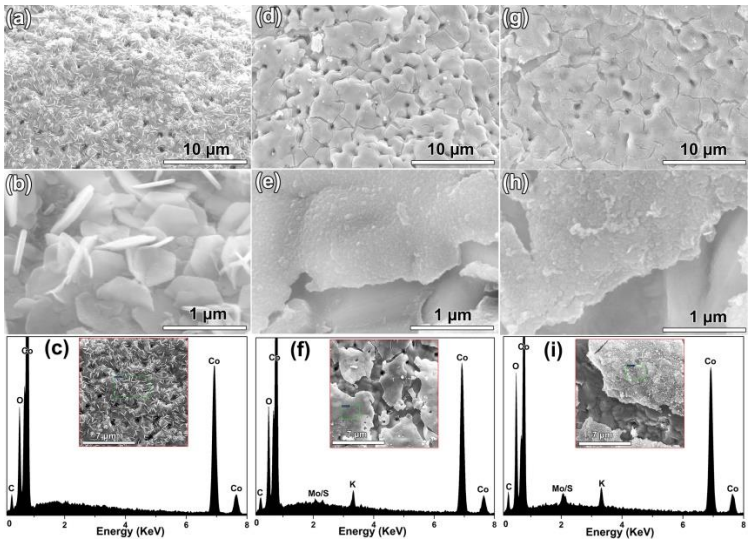

Fig. 7. SEM images and EDX spectra of the bare Co foam (a-c), Co@MoS_2-500 (d-f) and Co@MoS_2-1000 electrodes (g-i) after continuous galvanostatic electrolysis under OER conditions for 100 h. The K peaks in (c, f, i) are originated from the residue of KOH electrolyte.

According to the above SEM, XRD, and Raman spectroscopy analyses of the tested Co@ MoS_2 electrodes, it is concluded that the degradation of Co@ MoS_2 in OER activity upon long term galvanostatic electrolysis may primarily result from the formation of insulating and catalytically inactive molybdenum oxides. This would happen more prominently at a high current density like 100 mA cm^{-2}, as evidenced in the CP test (Fig. 6a). On the other hand, the activity degradation might also stem from the loss of the physical contact of the MoS_2 NC film with the underneath Co foam after the extended OER test, given that the film undergoes large structural deformation during the transformation to molybdenum oxide, particularly at a high current density. Notwithstanding their degradation, the Co@ MoS_2 electrodes

are still more active than the bare Co foam even after the long-term CP test (Fig. 6a and S9, ESI†). We hypothesize that there may exist many under-coordinated Mo moieties that expedite the turnover of hydroxyl groups. However, further investigation will be needed to clarify the actual mechanism.

In summary, we have deposited ultrafine MoS_2 nanocrystals on the entire surface of porous Co foam electrodes through atomic layer deposition. The as-obtained integrated Co@ MoS_2 electrode with an optimal MoS_2 loading exhibits outstanding catalytic activity towards the oxygen evolution reaction in an alkaline solution, showing a significant cathodic shift of 200 mV in the onset potential with respect to that of the bare Co foam and requiring only a small overpotential of 270 mV to deliver a current density of 10 mA cm^{-2}, favourably comparing to that of many sulfide OER catalysts as well as some state-of-the-art noble metal catalysts reported in the literature. Significantly, Co@ MoS_2 electrodes show excellent long-term stability at both a low current density relevant to solar water splitting and a high current density relevant to industrial water electrolysis. Given that ALD is a versatile technique enabling conformal deposition of MoS_2over high aspect-ratio nanostructures, the approach reported here holds substantial promise for use not only in electrochemical water splitting but also in coupling MoS_2 electrocatalysts with nanostructured semiconductor photoelectrodes for solar water splitting.

Acknowledgements

L. F. Liu acknowledges the support of the FCT Investigator grant (no. IF/01595/2014) and the Exploratory grant (No. IF/01595/2014/CP1247/CT0001) from the Portuguese Foundation of Science & Technology (FCT). D. H. Xiong and W. Li are thankful for the financial support from Marie Curie Action COFUND fellowships (NanoTrainforGrowth, Grant Agreement no. 600375) under the FP7 framework. D. H. Xiong also acknowledges the financial support from the China Postdoctoral Science Foundation (No. 2015 T80847). This work was partly funded by the European Commission Horizon 2020 project “CritCat” (Grant Agreement No. 686053).

References

1 - X. X. Zou and Y. Zhang, Chem. Soc. Rev., 2015, 44, 5148–5180.

2 - C. C. McCrory, S. Jung, I. M. Ferrer, S. M. Chatman,J. C. Peters and T. F. Jaramillo, J. Am. Chem. Soc., 2015, 137, 4347–4357.

3 - J. Wang, W. Cui, Q. Liu, Z. Xing, A. M. Asiri and X. Sun,Adv. Mater., 2016, 28, 215–230.

4 - F. Wang, T. A. Shifa, X. Zhan, Y. Huang, K. Liu, Z. Cheng,C. Jiang and J. He, Nanoscale, 2015, 7, 19764–19788.

5 - J. R. McKone, S. C. Marinescu, B. S. Brunschwig,J. R. Winkler and H. B. Gray, Chem. Sci., 2014, 5, 865–878.

6 - B. Martindale and E. Reisner, Adv. Energy Mater., 2016, 6,1502095.

7 - H. Jin, J. Wang, D. Su, Z. Wei, Z. Pang and Y. Wang, J. Am.Chem. Soc., 2015, 137, 2688–2694.

8 - J. R. Swierk, S. Klaus, L. Trotochaud, A. T. Bell andT. D. Tilley, J. Phys. Chem. C, 2015, 119, 19022–19029.

9 - H. Li, Y. Shao, Y. Su, Y. Gao and X. Wang, Chem. Mater.,2016, 28, 1155–1164.

10 - P. Ganesan, M. Prabu, J. Sanetuntikul and S. Shanmugam,ACS Catal., 2015, 5, 3625–3637.

11 - Y. Liu, C. Xiao, M. Lyu, Y. Lin, W. Cai, P. Huang, W. Tong, Y. Zou and Y. Xie, Angew. Chem. Int. Ed., 2015, 127, 11383–11387.

12 - C. Tang, N. Cheng, Z. Pu, W. Xing and X. Sun, Angew. Chem., Int. Ed., 2015, 54, 9351–9355.

13 - J. Masud, A. T. Swesi, W. P. Liyanage and M. Nath, ACS Appl. Mater. Interfaces, 2016, 8, 17292–17302.

14 - L. A. Stern, L. G. Feng, F. Song and X. L. Hu, Energy Environ. Sci., 2015, 8, 2347–2351.

15 - X. G. Wang, W. Li, D. H. Xiong and L. F. Liu, J. Mater. Chem. A, 2016, 4, 5639–5646

16 - A. Mendoza-Garcia, D. Su and S. H. Sun, Nanoscale, 2016,8, 3244–3247.

17 - X. Wang, W. Li, D. Xiong, D. Y. Petrovykh and L. Liu, Adv.Funct. Mater., 2016, 26, 4067–4077.

18 - N. Jiang, B. You, M. L. Sheng and Y. J. Sun, Angew. Chem.,Int. Ed., 2015, 54, 6251–6254.

19 - D. Xiong, X. Wang, W. Li and L. Liu, Chem. Commun., 2016,52, 8711–8714.

20 - W. Li, X. F. Gao, X. G. Wang, D. H. Xiong, P. P. Huang,W. G. Song, X. Q. Bao and L. F. Liu, J. Power Sources, 2016, 330, 156–166.

21 - Y. Yan, B. Xia, Z. Xu and X. Wang, ACS Catal., 2014, 4, 1693–1705.

22 - T. F. Jaramillo, K. P. Jorgensen, J. Bonde, J. H. Nielsen, S. Horch and I. Chorkendorff, Science, 2007, 317, 100– 102.

23 - Y. Li, J. Wang, X. Tian, L. Ma, C. Dai, C. Yang and Z. Zhou, Nanoscale, 2016, 8, 1676–1683.

24 - D. Merki, S. Fierro, H. Vrubel and X. L. Hu, Chem. Sci., 2011, 2, 1262–1267.

25 - W. Li, X. G. Wang, D. H. Xiong and L. F. Liu, Int. J. Hydrogen Energy, 2016, 41, 9344–9354.

26 - X. Geng, W. Sun, W. Wu, B. Chen, A. Al-Hilo, M. Benamara, H. Zhu, F. Watanabe, J. Cui and T. P. Chen, Nat. Commun., 2016, 7, 10672.

27 - J. Wu, M. Liu, K. Chatterjee, K. P. Hackenberg, J. Shen, X. Zou, Y. Yan, J. Gu, Y. Yang, J. Lou and P. M. Ajayan, Adv. Mater. Interfaces, 2016, 3, 1500669.

28 - H. Zhu, J. Zhang, R. Yanzhang, M. Du, Q. Wang, G. Gao, J. Wu, G. Wu, M. Zhang, B. Liu, J. Yao and X. Zhang, Adv. Mater., 2015, 27, 4752–4759.

29 - J. Zhang, T. Wang, D. Pohl, B. Rellinghaus, R. H. Dong, S. H. Liu, X. D. Zhuang and X. L. Feng, Angew. Chem., Int. Ed., 2016, 55, 6701–6706.

30 - K. Yan and Y. Lu, Small, 2016, 12, 2975–2981.

31 - M. Knez, K. Nielsch and L. Niinisto, Adv. Mater., 2007, 19, 3425–3438

32- L. K. Tan, B. Liu, J. H. Teng, S. F. Guo, H. Y. Low andK. P. Loh, Nanoscale, 2014, 6, 10584–10588.

33- Z. Y. Jin, S. Shin, D. H. Kwon, S. J. Han and Y. S. Min, Nanoscale, 2014, 6, 14453–14458.

34- S. Shin, Z. Y. Jin, D. H. Kwon, R. Bose and Y. S. Min, Langmuir, 2015, 31, 1196–1202.

35- D. H. Kwon, Z. Y. Jin, S. Shin, W. S. Lee and Y. S. Min, Nanoscale, 2016, 8, 7180.

36 - S. McDonnell, A. Azcatl, R. Addou, C. Gong, C. Battaglia, S. Chuang, K. Cho, A. Javey and R. M. Wallace, ACS Nano, 2014, 8, 6265–6272.

37 - J. Kibsgaard, Z. Chen, B. N. Reinecke and T. F. Jaramillo, Nat. Mater., 2012, 11, 963–969.

38 W. Zhao, C. Zhang, F. Geng, S. Zhuo and B. Zhang, ACS Nano, 2014, 8, 10909–10919.

39- Y. Liu, C. Xiao, M. Lyu, Y. Lin, W. Cai, P. Huang, W. Tong, Y. Zou and Y. Xie, Angew. Chem., Int. Ed., 2015, 127, 11383– 11387.

40 - B. K. Barman and K. K. Nanda, Dalton Trans., 2016, 45, 6352–6356.

41 - X. Wang, Y. Zheng, J. Yuan, J. Shen, A. J. Wang, L. Niu and S. Huang, Electrochim. Acta, 2016, 212, 890–897.

42- S. Jung, C. C. L. McCrory, I. M. Ferrer, J. C. Peters and T. F. Jaramillo, J. Mater. Chem. A, 2016, 4, 3068–3076.

43 - C. C. L. McCrory, S. Jung, J. C. Peters and T. F. Jaramillo, J. Am. Chem. Soc., 2013, 135, 16977–16987.

44 - W. Zhu, X. Yue, W. Zhang, S. Yu, Y. Zhang, J. Wang and J. Wang, Chem. Commun., 2016, 52, 1486–1489.

45 - A. Sivanantham, P. Ganesan and S. Shanmugam, Adv. Funct. Mater., 2016, 26, 4661.